

Determination of target-oriented parameters for computation of curvature attributes

Lee Hunt¹, Bahaa Beshry¹, Satinder Chopra², and Cole Webster¹

Abstract

The application of curvature attributes on seismic horizons or 3D seismic volumes has been discussed in the literature in several ways. Such discussion largely ignores the detail of parameter selection that must be made by the working interpreter or the expert processor. Parameter selection such as window size and filtering methods for seismic curvature estimates have not been extensively compared in the literature and have never been validated using quantitative ground truthing to log or drilling data. Of even greater relevance to the interpreter is the lack of discussion of curvature parameters as they are relevant to interpretive and operational concerns. We focus on the seismic most-positive curvature attribute, its parameterization, and filtering for the overpressured tight sand target in the Falher F formation of the deep basin of Alberta, Canada. This sand has numerous natural fractures that constitute an occasional drilling hazard due to mud losses. Various parameterizations on horizon- and volume-based curvature extractions are made and examined in the context of the drilling results of four horizontal wells, one of which has image log fracture density along the lateral portion of the well. We compared different lateral (and vertical where applicable) window sizes in the initial curvature estimates, as well as different postcurvature filtering approaches including unfiltered, Gaussian-filtered, and Fourier-filtered products. The different curvature attribute estimates have been evaluated by way of map comparisons, cross-section seismic line comparisons, and correlations with the upscaled fracture density log data. We found that our horizon-based estimates of positive curvature suffered from mechanical artifacts related to the horizon picking process, and the volume-based methods were generally superior. Of the volume-based methods, we found that the Fourier-filtered curvature estimates were the most stable through smaller analysis windows. Gaussian-filtering methods on volumetric curvature gave results of varying quality. Unfiltered volumetric curvature estimates were only stable when very large time windows were used, which affected the time localization of the estimate. The comparisons give qualitative and quantitative perspective regarding the best parameters of curvature to predict the key properties of geologic target, which in this case are the potentially hazardous natural fractures within the overpressured Falher F sandstone.

Introduction

Curvature has long been used by geologists to predict the density of natural fractures from outcrops (Murray, 1968). Sand box experiments show that the correlations between curvature and strain can be significant (Keating and Fischer, 2008), which is supportive of the curvature-strain-natural fracture supposition inherent in the use of curvature to predict natural fractures. This work does not include a comparison of different curvature parameters. Hennings et al. (2000) show a significant correlation to map-based total curvature and fracture intensity as measured along an outcrop. This study is significant for the use of curvature for fracture prediction in general, but it is not expository for the question of its parameterization for the same purpose in

the seismic medium. Seismic horizon-based curvature estimates have been shown to be potentially effective in the same manner as that of geologic map approaches. This was followed by volumetric seismic curvature, which has largely replaced horizon-based curvature estimates (Chopra and Marfurt, 2007) perhaps due to the elimination of picking a horizon in data not well-suited to horizon picking, or not having a pickable horizon in our zone of interest. Chopra and Marfurt's (2007) results are qualitative in nature, and they do not reference drilling results or other hard validating evidence, nor do they explore or compare different window sizes for the horizon-based or volumetric methods of curvature estimation. Hunt et al. (2010) find statistically significant correlations between the volumetric most-positive curvature

¹Jupiter Resources Inc., Mimir's Well Exploration Corp., Calgary, Alberta, Canada. E-mail: leehunt@telusplanet.net; bbeshry@jupiterresources.com; cwebster@jupiterresources.com.

²TGS, Arcis Seismic Solutions, Calgary, Alberta, Canada. E-mail: satinder.chopra@tgs.com.

Manuscript received by the Editor 9 November 2017; revised manuscript received 4 January 2018; published ahead of production 08 March 2018; published online 25 April 2018. This paper appears in *Interpretation*, Vol. 6, No. 2 (May 2018); p. T485–T498, 16 FIGS., 1 TABLE.

<http://dx.doi.org/10.1190/INT-2017-0202.1>. © 2018 Society of Exploration Geophysicists and American Association of Petroleum Geologists. All rights reserved.

and the natural fracture density indicated from high-resolution image log data along horizontal wells. In another study, [Hunt et al. \(2011\)](#) combine the curvature and Young's modulus to quantitatively predict natural fractures as measured from high-resolution image log data along the vertical and horizontal wells. In both [Hunt et al. \(2010, 2011\)](#) papers, only one window size and filtering technique is used for the curvature estimates. [Al-Dossary and Marfurt \(2006\)](#) show the importance of Fourier filtering on volumetric curvature. Their approach has gained widespread acceptance, although they do not estimate its advantages over other filtering methods through any qualitative or quantitative validation techniques with well performance or log data. There are other methods for generation and filtering of curvature attribute that are available in our industry; however, these methods are not compared with each other with validating information from drilling or well-log data anywhere in the literature. The same lack of quantitative validation is true for the curvature window size. We present here a quantitative and qualitative comparison of curvature parameterization and filtering on the prediction of natural fractures. We use data from the drilling history of several horizontal wells and high-resolution image log-based fracture density data from one horizontal well to make our evaluation objective and scientific.

The Falher F tight sandstone of the deep basin in Alberta, Canada, is gas charged, deeply buried at approximately 3200 m true vertical depth, and overpressured with gradients of approximately 14.5 KPa/m. The net horizontal stress in the Falher F is quite low,

which makes the drilling mud window narrow. Compounding this operational challenge is the fact that the sand has abundant natural fractures that can lead to mud losses or gas kicks depending on the management of the mud weight. Either the loss of too much mud or the uncontrolled production of too much gas can lead to catastrophic operational failure in this overpressured system.

Case study

The Falher F target formation in the study area is interpreted to be an incised valley fill and consists of a series of stacked fluvial channels. These channels are composed of very clean, quartz-rich, medium-grained sandstones. This quartz-rich mineral composition of the Falher F is likely to lead to high relative natural fracture density ([Nelson, 2001](#)). Given the overpressuring and low net horizontal stress, The Falher F formation is paradoxically at risk for high mud losses and uncontrolled gas releases. The prediction of natural fractures within the reservoir is therefore operationally critical. We assessed the best curvature parameterization as being the one in which the hazard presented by the natural fractures was most clearly interpreted from map and line views, and they had the highest correlation with fracture density as estimated in horizontal wells. We argue that the interpretive objective, or target, should generally be given primary consideration when choosing curvature parameters. Our study area is depicted in Figure 1, and it has four horizontal wells, depicted as wells 0, A, B, and C. Well 0 and well A encountered numerous open fractures,

suffered uncontrolled losses of drilling mud, and were abandoned due to related operational concerns. Well C had no discernible operational issues, although some fracture infill material was reported by the wellsite team. The operational failure of wells 0 and A suggests that a high density of fractures must exist near the end of those wellbores. Well B has image log fracture density data, which is displayed in Figure 1a. Figure 1b shows a larger area around the wells with two evaluation lines displayed in white. Both seismic lines are depicted in Figure 2, in which the zone of interest is marked at the shallow level. A reasonable but uncertain interpretation of the events from these wells is that a trend of high-density fractures exists in a curve or line going from the toe of well 0, past the high fracture density area of well B, to the toe of well A. This feature is anticlinal in nature, and it can be evaluated with estimates of most-positive curvature. The lateral length of well B is just more than 1500 m. Exact scales and the direction of north are not given to protect the confidentiality of the data.

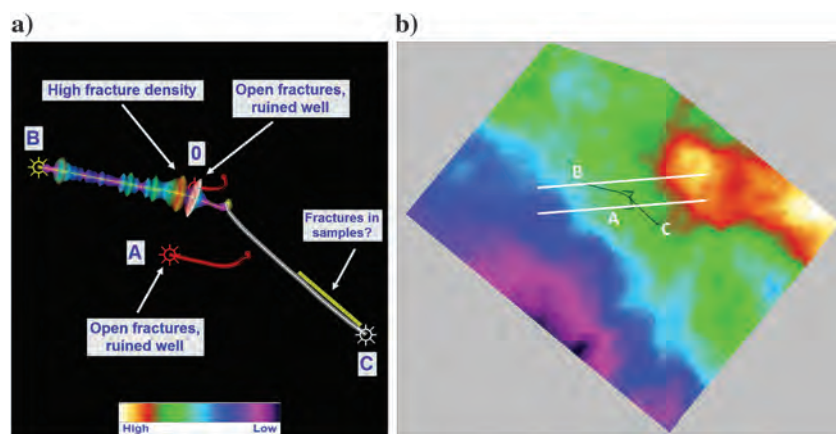


Figure 1. Maps depicting the key elements of the case study. (a) A 3D perspective view of wells 0, A, B, and C. Well B has an image log estimate of fracture density. The fracture density is displayed as rings whose size is linearly proportional to density. Well 0 and well A encountered numerous open fractures, suffered uncontrolled losses of drilling mud, and were abandoned due to related operational concerns. Well C had no discernible operational issues, although some fracture infill material was reported by the wellsite team. (b) A time structure map of the Falher F for a portion of the study area. The two seismic lines are shown as the white straight lines. The toe of well A is indicated by an arrow, and it coincides with a structural feature. All seismic data images are arbitrarily cut and rotated, with the exact scales hidden, to protect the confidentiality of the data. The same color bar is used for all images except for Figures 13–15 (data courtesy of SEI, Canada).

Curvature

Curvature refers to the degree of bending of a reflection surface, and it can be measured as the rate of change of the curved reflection in a given direction. This would suggest that in the simplest way, one could calculate curvature by computing the first and second derivatives of the x - and y -components of the surface. The first and second derivatives of a curve can be approximated by calculating the derivatives of a continuous function and fitted to the given curve. The finite-difference approach to derivative estimation approximates a curved segment with a straight line and then differentiating the line. Similarly, the curved segment can be approximated with parabolas by a least-squares approach. Alternatively, the curvature of a curved reflection at a given point can be measured as the curvature of an osculating circle at that point. The reciprocal of the radius of the osculating circle defines the curvature at that point. A sharply curved reflection would be associated with a smaller osculating circle (smaller radius), and thus have higher curvature, and vice versa.

Such a simple definition of curvature has been extended to curvature computation on interpreted horizons (Roberts, 2001) on a 3D seismic volume, as well as volumetric computation of curvature as a whole (Al-Dossary and Marfurt, 2006).

Horizon-based curvature

The surface computation of curvature involves fitting a quadratic surface to the mapped horizon using a least-squares regression and nine sample points (eight neighbors around a given point).

A quadratic polynomial may be written as

$$z(x, y) = a \frac{\partial^2 z}{\partial x^2} + b \frac{\partial^2 z}{\partial x \partial y} + c \frac{\partial^2 z}{\partial y^2} + d \frac{\partial z}{\partial x} + e \frac{\partial z}{\partial y} + f, \quad (1)$$

and it has six coefficients. When nine sample points are used for the computation of curvature, it results in an overdetermined system when the solution is sought by the least-squares regression method. Different measures of curvature can then be written in terms of the six coefficients, as is shown by Roberts (2001).

Volumetric computation of curvature

For extension to volumetric computation of curvature, equation 1 may be written as

$$z(x, y) = a \frac{\partial p}{\partial x} + \frac{b}{2} \left(\frac{\partial p}{\partial y} + \frac{\partial q}{\partial x} \right) + c \frac{\partial q}{\partial y} + dp + eq + f, \quad (2)$$

where p and q are the volumetric estimates of the inline and crossline components of dip, respectively. They are now used to approximate $p \equiv \partial z / \partial x$ and $q \equiv \partial z / \partial y$.

Per Al-Dossary and Marfurt (2006), evaluating the polynomial equation at $x = 0$, $y = 0$ yields

$$d = p,$$

$$e = q,$$

$$\frac{\partial^2 z}{\partial x^2} = 2a = \frac{\partial p}{\partial x},$$

$$\frac{\partial^2 z}{\partial x \partial y} = b = \frac{1}{2} \left(\frac{\partial p}{\partial y} + \frac{\partial q}{\partial x} \right), \quad \text{and}$$

$$\frac{\partial^2 z}{\partial y^2} = 2c = \frac{\partial q}{\partial y}. \quad (3)$$

The derivatives in the last three equations are computed numerically so that a , b , and c can be determined. Of all the available curvature measures, Chopra and Marfurt (2007) recommend the most-positive curvature and most-negative curvature attributes because they are the easiest to understand intuitively.

Roberts (2001) has given the following expression for computation of the most-positive curvature:

$$K_{\text{Pos}} = (a + b) + \sqrt{(a - b)^2 + c^2}, \quad (4)$$

where a , b , and c are the coefficients given in equations 1 and 2.

As we noted above, curvature is a function of the first derivatives of the inline dip p and crossline dip q . In the method of Fourier filtering, Al-Dossary and Marfurt (2006) introduce a fractional index (α)-based multispectral estimation of curvature. The derivative in $\partial/\partial x$ in the Fourier domain is equivalent to multiplying the spectrum by (ik) , but Al-Dossary and Marfurt (2006) introduce a fractional index α such that the spectrum gets multiplied by it. The smaller values of α yield the long wavelength estimates of curvature, and the larger values yield the short wavelength. The inverse Fourier transform allows the generation of 3D convolution operator, which is convolved with p and q to obtain filtered versions of $\partial p / \partial x$, $\partial p / \partial y$, $\partial q / \partial x$, and $\partial q / \partial y$. Such estimates have their applications: the long wavelength being suitable for obtaining the gross definitions of the geometric features and the short wavelength for extracting the finer details and thus more resolved images.

As we mentioned above, the computation of curvature requires estimation of the first- and second-order derivatives. Estimation of these derivatives is done from the seismic data using a set of samples in the spatial direction for horizon-based curvature or a cuboid of data for its volumetric computation. Once these derivatives are in place, the polynomial of derivatives is solved for different curvature measures. Usually, the computation of derivatives or curvature measures is carried out on preconditioned seismic data such that the random noise in the data is minimized. Alternatively, the output curvature estimates may be filtered so as to reduce any jitter of lineament detail that is blown up with the computations.

The different commercial seismic data interpretation software packages available in our industry offer variations in the computation of the polynomials in terms of parameters in the x -, y -, and z -directions. The filtering may be inherent in the workflow in some software packages.

We examined the following parameter variations:

- 1) horizon versus volumetric estimation of curvature
- 2) size of the cuboid used for estimation of derivatives (x , y in number of samples and z in ms)
- 3) type of filtering applied to curvature, if at all. We specifically compare unfiltered, Gaussian filtering, and Fourier filtering.

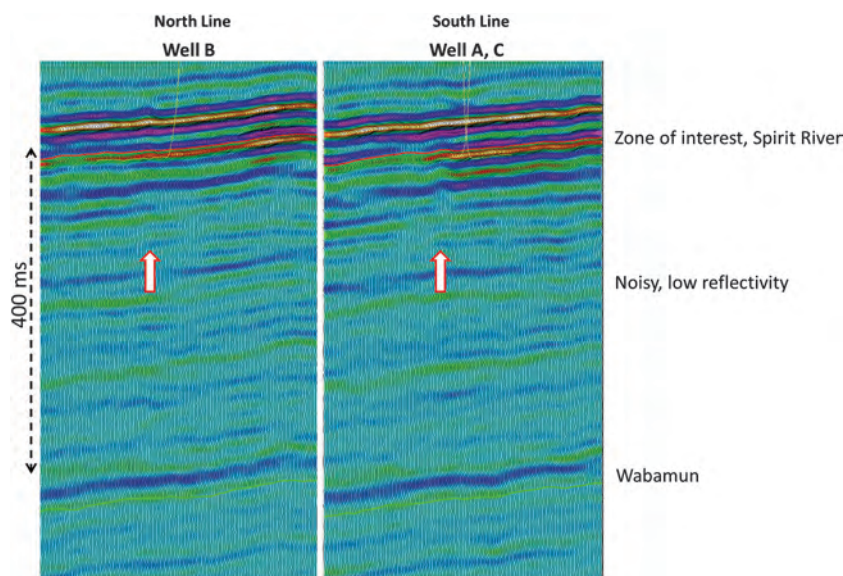


Figure 2. Segments of the north and south lines shown in Figure 1b from the 3D seismic data volume. The zone of interest is marked on the sections, and so are a couple of horizons (Spirit River and Wabamun). The equivalent segments of these lines are displayed in the subsequent figures, from different curvature attribute volumes generated with different algorithms and parameters (data courtesy of SEI, Canada).

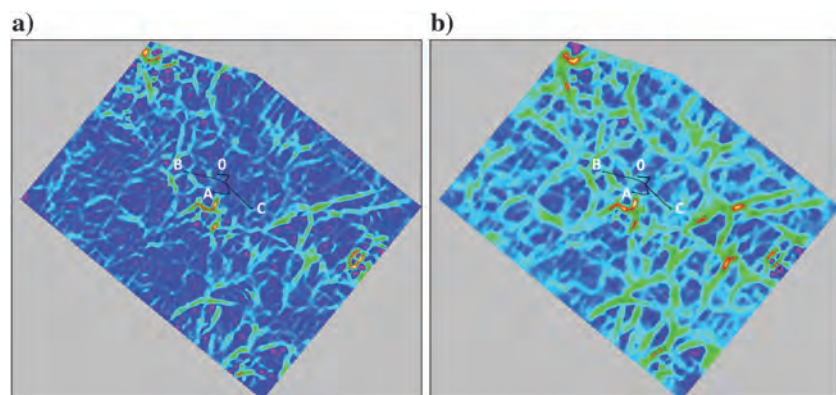


Figure 3. Horizon-based most-positive curvature computed on the Falher F surface in the study area using (a) 9×9 and (b) 17×17 samples. Using a larger number of samples in the curvature computation irons out the curvature lineament detail on the displays (data courtesy of SEI, Canada).

The estimates of the most-positive curvature were derived from four separate industrially offered applications. Qualitative comparisons were made based on the map interpretation of curvature and the two lines described in Figure 1. Quantitative evaluation of curvature was made by linear regression with the upscaled fracture density from the image log of the 1500 m long lateral of well B.

Diffraction imaging

Besides the traditional attributes such as coherence and curvature, diffraction imaging has been promoted as an alternative tool for mapping discontinuities corresponding to faults and fracture swarms using seismic data. Diffractions are generated as a direct seismic wavefield response to intermediate-scale discontinuities (Landa, 2012) in the subsurface. Consequently, the amplitudes of diffracted waves are smaller than those of the reflected waves. Methods have been developed for extraction of the diffractions from the overall seismic wavefield and then to image them (Fomel et al., 2007; Koren and Ravve, 2011; Klovov and Fomel, 2012).

A diffraction imaging workflow was applied to the same seismic data; however, it must be noted that the processing flow for diffraction imaging differs significantly from the processing sequence used to produce an optimal stack for curvature analysis. The diffraction imaging workflow has much less noise attenuation, particularly less FXY noise attenuation. The reasons for this are the delicacy of the diffractions, which must be preserved through processing. Some might argue that the significant differences in processing flow invalidate the comparison. This argument would miss the true value of using the curvature and diffraction imaging analysis. The information being extracted from each method is fundamentally different; thus, different processing flows should be expected.

Figure 3 illustrates two different horizon-based curvature estimates. Figure 3a shows Falher F level horizon-based 9×9 most-positive curvature, whereas Figure 3b illustrates a 17×17 sized estimate. In contrast, Figure 4 shows a Falher F level horizon slice from the diffraction imaging volume. This image is very noisy, and the individual lineaments corresponding to fractures are an interpretive challenge of the most uncomfortable but familiar sort. The curvature and diffraction imaging horizon slices

have similarities and differences, which are of logical interest.

Hunt (2013) describes virtually all seismic interpretation as an inductive exercise, with data from various seismic properties forming weak evidence for an argument, or conclusion. The diffraction imaging data are an

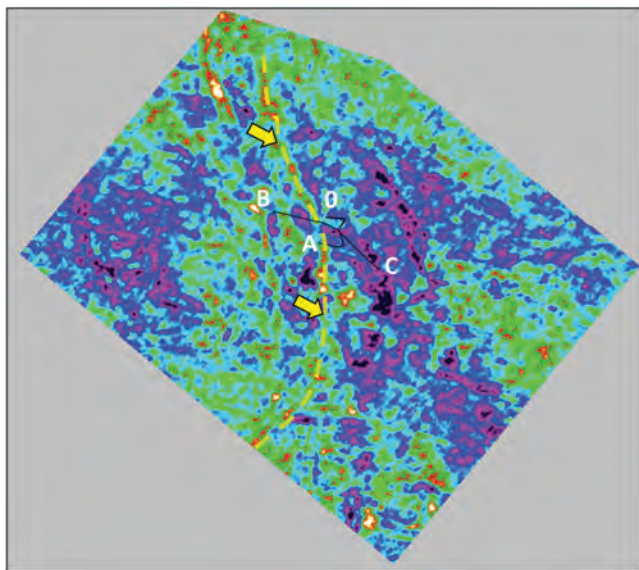


Figure 4. Horizon slice from the diffraction imaging volume for the Falher F surface. Interpretation on this slice is somewhat confusing and, so, difficult (data courtesy of SEI, Canada).

uncomfortable exercise because its relationship to fractures is not as clear, unique, or accurate as we would like, and it is a familiar exercise because the lack of accuracy, uniqueness, or clarity is sadly typical. We have some reason to believe that the diffraction imaging data could be useful for indicating fractures as well as edges, but we are certain that interpreting the diffraction imaging data to make predictions is challenging. The same could be said for curvature data. Both properties have challenges in their use, and we suggest that thinking of them as “alternative” fracture predictors is irrational: These two attributes should be considered as complementary techniques. Hunt (2013) offers the idea that using different independent seismic attributes together makes rational sense as an inductive v-argument and that if all (or many) attributes make similar predictions, then interpretive confidence is higher. This structure from logic supports the common use we make of multiattributes, whether it is through crossplotting, corendering, or multivariate analysis.

The relevance of the diffraction imaging data in Figure 4 is the arcuate feature indicated by the yellow arrow, which intersects the ends of well 0 and well A, where catastrophic mud losses occurred that we attribute to open fractures. The arcuate feature is interpreted as belonging to a low relief fault or an open fracture swarm caused by structural deformation (a small fold). This arcuate feature may be compared with the curvature maps to follow, with some prejudice being given to curvature parameterizations wherein this feature is most prominent.

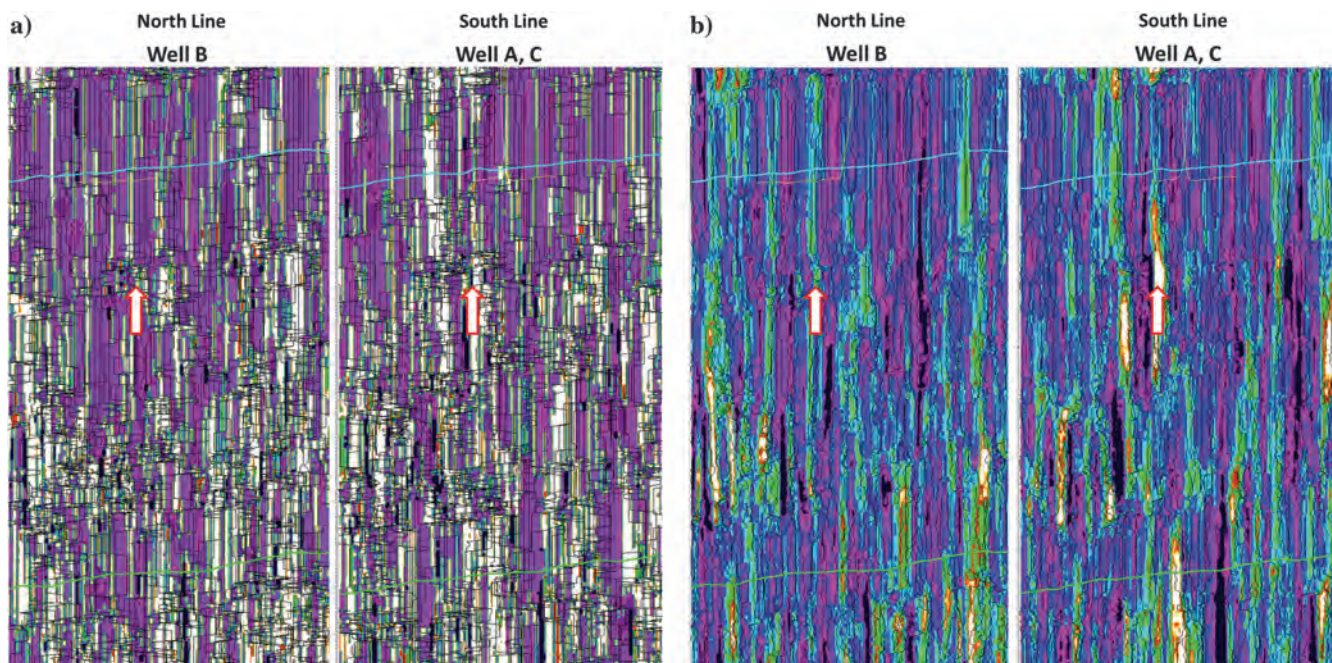


Figure 5. Segments of the north and south lines shown in Figure 1b from the most-positive curvature volume generated using a linear-weighted algorithm, and using (a) three samples in the inline and crossline directions and 98 ms as the time window, and (b) five samples in the inline and crossline directions and 98 ms as the time window. Increasing the number of samples in the spatial direction reduces the level of noise on the curvature displays. It might be argued that both these results are too noisy (data courtesy of SEI, Canada).

Results

Only a small subset of the results is shown in this paper, although the comparison was carried out on the

vertical lines as well as horizontal displays from all of the attribute volumes.

In Figure 3, we show a comparison of horizon-based most-positive curvature computed on the Fahler F sur-

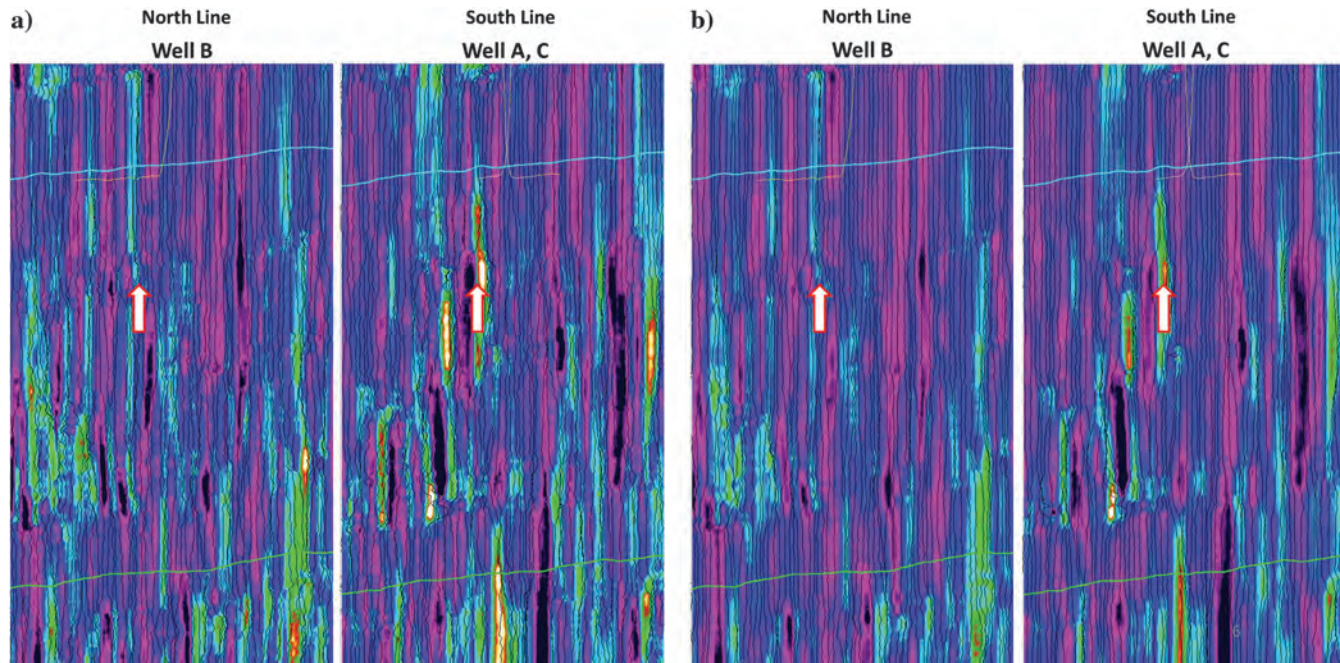


Figure 6. Segments of the north and south lines shown in Figure 1b from the most-positive curvature volume generated using a linear-weighted algorithm and using (a) seven samples in the inline and crossline directions and 98 ms as the time window and (b) nine samples in the inline and crossline directions and 98 ms as the time window. Increasing the number of samples in the spatial direction smooths out the detail on the curvature displays, and it slightly reduces the noise level. The 7×7 cuboid size might be argued as the minimum stable size for unfiltered curvature estimates in this example (data courtesy of SEI, Canada).

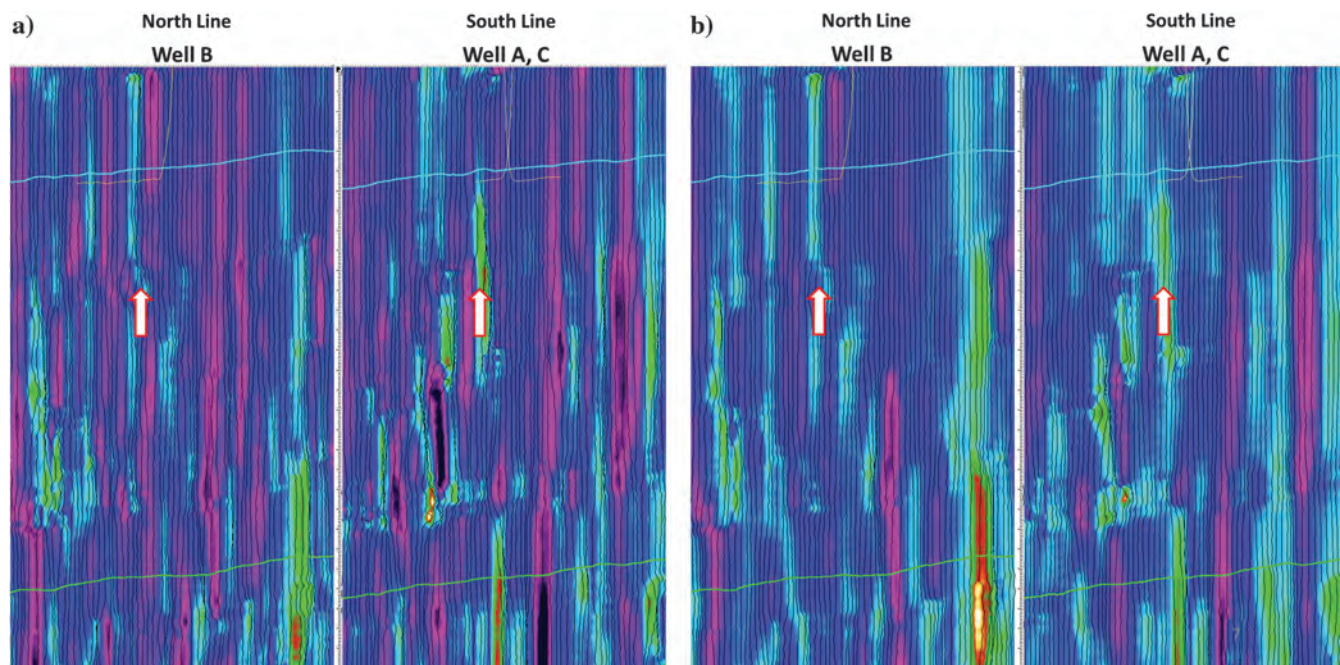


Figure 7. Segments of the north and south lines shown in Figure 1b from the most-positive curvature volume generated using a linear-weighted algorithm and using (a) 11 samples in the inline and crossline directions and 98 ms as the time window and (b) 17 samples in the inline and crossline directions and 98 ms as the time window. Increasing the number of samples in the spatial direction smooths out the detail on the curvature displays (data courtesy of SEI, Canada).

face using 9×9 and 17×17 spatial samples. The display with 17×17 samples loses the fine lineament detail that is seen on the display with 9×9 samples, even though some lineament patterns show up better on the former.

In Figure 4, we show an equivalent horizon display as shown in Figure 3, but from the diffraction imaging volume. The diffraction imaging data are noisy and suffer from interpretational challenges;

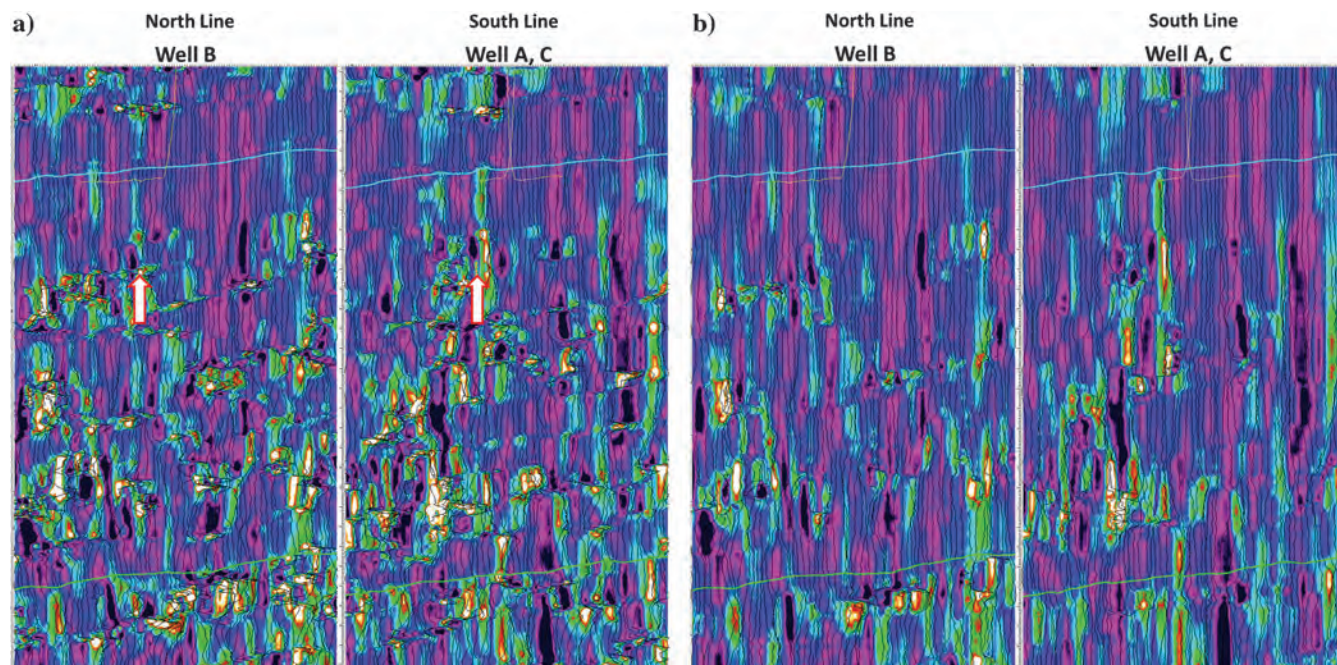


Figure 8. Segments of the north and south lines shown in Figure 1b from the most-positive curvature volume generated using a linear-weighted algorithm, keeping the spatial samples as fixed at 9×9 , and using (a) 22 ms as the time window and (b) 46 ms as the time window. Increasing the number of samples in the temporal direction smooths out the detail on the curvature displays, but it reduces the amount of noise in the estimate. Curvature estimates from both these time windows were deemed too noisy (data courtesy of SEI, Canada).

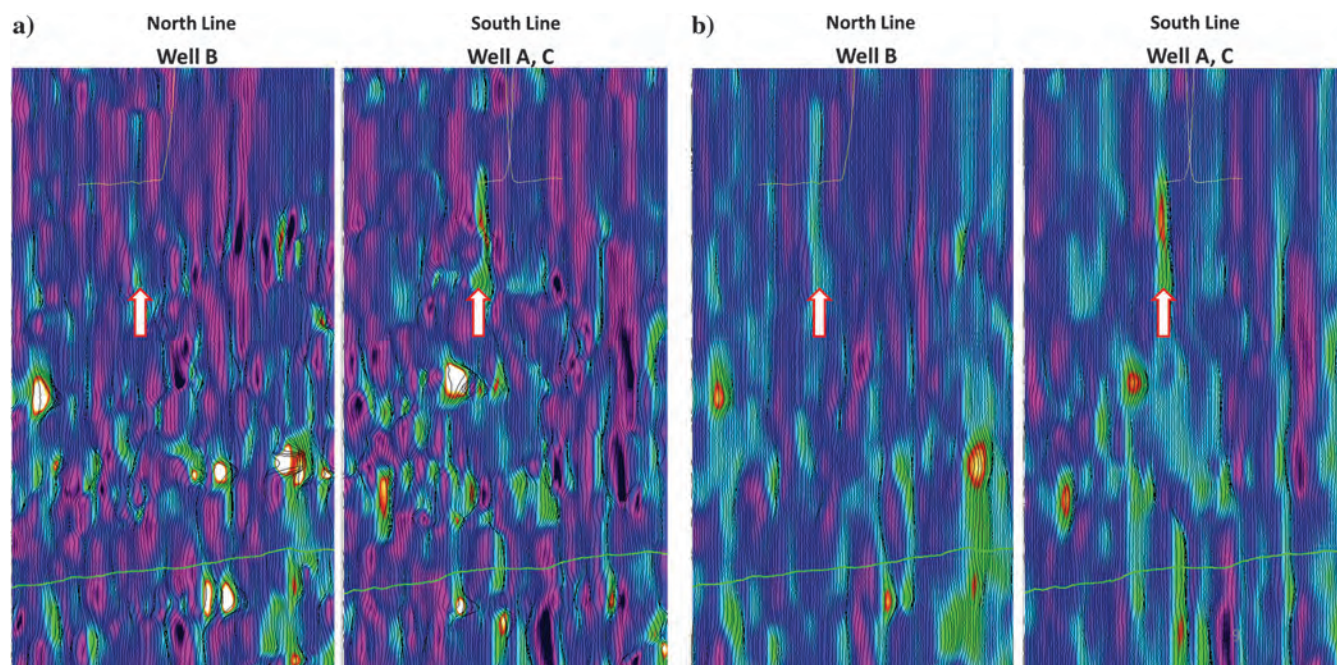


Figure 9. Segments of the north and south lines shown in Figure 1b from the most-positive curvature volume generated using a Gaussian-weighted algorithm using (a) 1×5 and (b) 2×9 . Using higher values of the filtering parameters smooths out the detail on the curvature displays (data courtesy of SEI, Canada).

however, it is a useful complement to the curvature analysis. Note the arcuate feature indicated by the yellow arrows, which intersects the ends of well 0 and well A, in which catastrophic mud losses occurred, which we attribute to open fractures. This arcuate feature may be compared with the subsequent curvature.

Going back to the horizon-based curvature maps of Figure 3, we may be suspicious that the dominant features on both maps (just below well A) could be pick-related artifacts because they do not conform to the arcuate feature interpreted from the diffraction imaging volume.

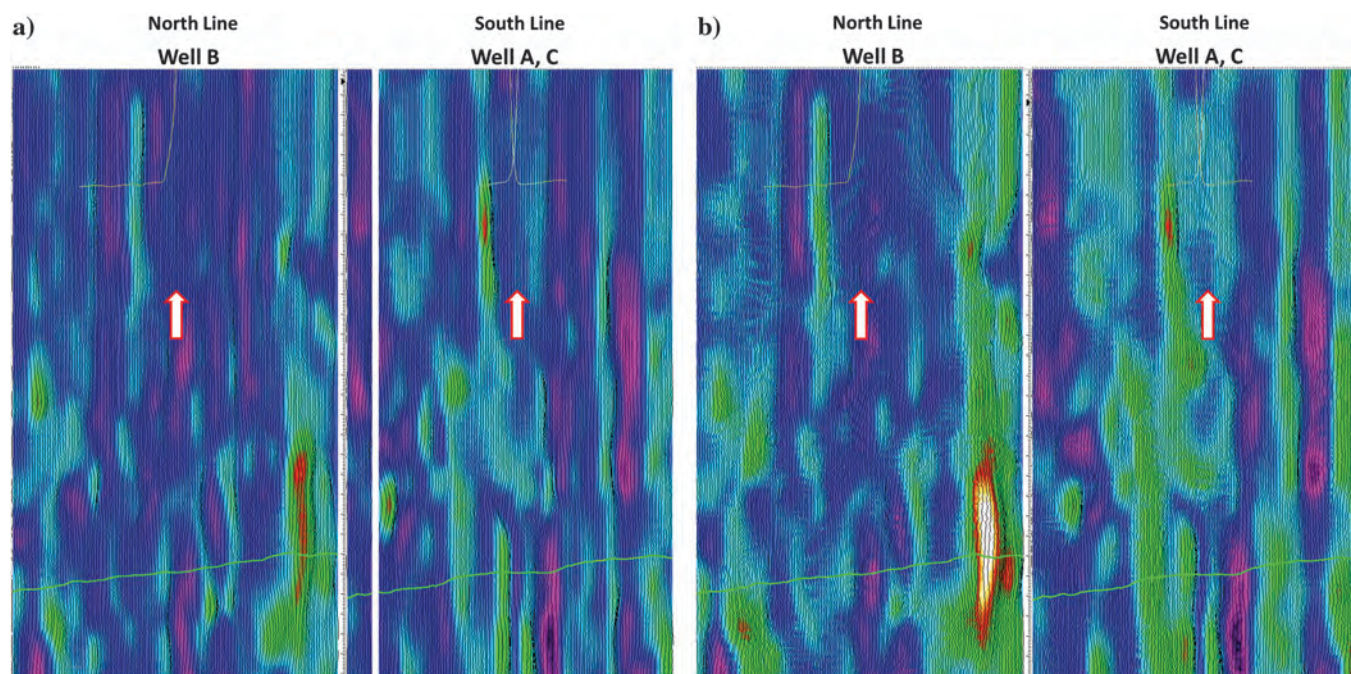


Figure 10. Segments of the north and south lines shown in Figure 1b from the most-positive curvature volume generated using a Gaussian-weighted algorithm using (a) 3×10 and (b) 5×10 . Using higher values of the filtering parameters smooths out the detail on the curvature displays (data courtesy of SEI, Canada).

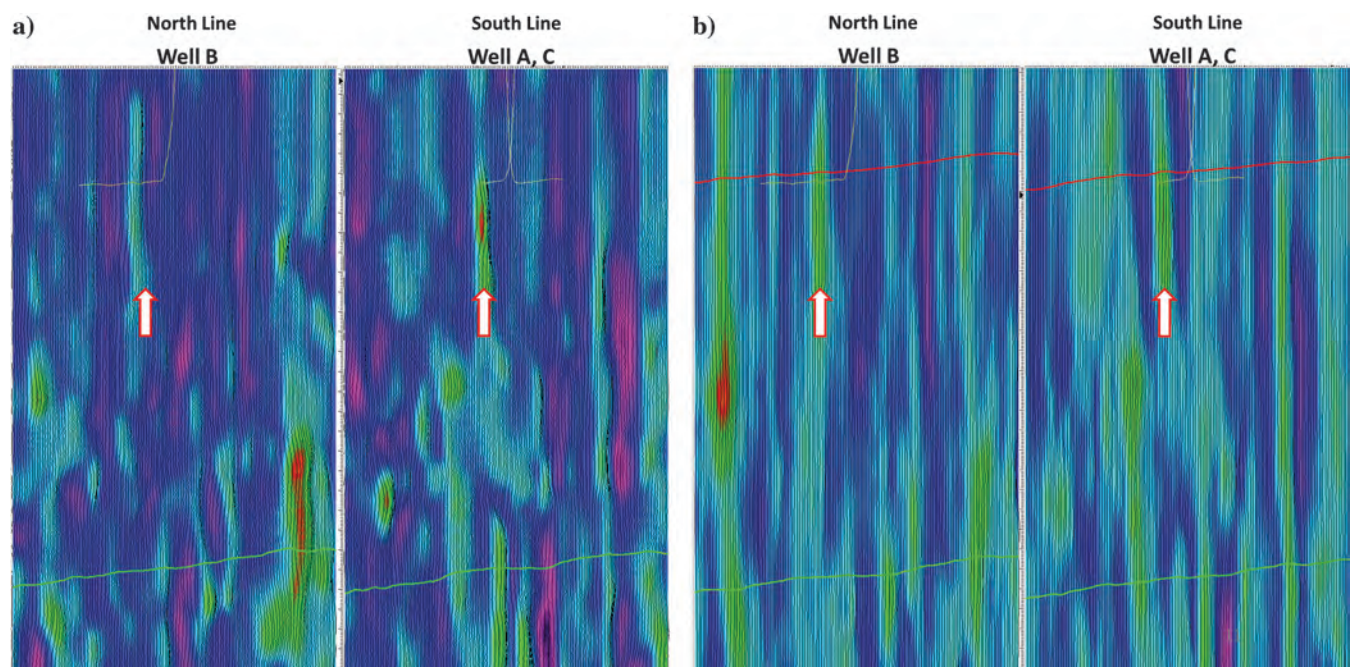


Figure 11. Segments of the north and south lines shown in Figure 1b from the most-positive curvature volume generated using a Fourier-filtering algorithm using an alpha value of (a) 0.2 and (b) 0.4. Using lower values of the alpha parameter smooths out the detail on the curvature displays (data courtesy of SEI, Canada).

Figure 2 shows the stack images of the two seismic lines as defined in Figure 1b. The zone of interest is the Spirit River, and it is denoted by a thin yellow horizon. This zone is generally, but not always, pickable. There are small-scale undulations on the Spirit River horizon. The scale of deformation at the Falher F zone is clearly very small; the features under discussion are subtle.

In Figures 5, 6, and 7, we show the two seismic lines drawn from the most-positive curvature attribute generated using a linear-weighted algorithm, and using 3 samples (Figure 5a), which is a noisy and unstable result, 5 samples (Figure 5b), 7 samples (Figure 6a), 9 samples (Figure 6b), 11 samples (Figure 7a), and 17 samples (Figure 7b) in the inline and crossline directions. In all these cases, the vertical window was kept constant at 98 ms. We note that increasing the number of samples in the spatial direction reduces noise but smooths out the detail on the curvature displays. A good trade-off size for stability versus resolution is in the 7×7 to 11×11 range.

Next, we fix the spatial samples at nine samples in the inline and crossline directions, and we use a time window of 22 ms (Figure 8a) and 46 ms (Figure 8b). Again, an increasing window in the temporal direction smooths out the detail in that direction. That said, it appears that the linear-weighted result requires very long time windows to achieve stability, which works against time localizing structural events. From the examples shown in Figures 5–8, we see that the minimum stable cuboid sizes for unfiltered most-positive curvature are quite large, and they are approximately $7 \times 7 \times 98$ ms in size.

We now turn to the Gaussian-weighted algorithm application, in which the parameterization is in terms of two parameters, the first defining a proxy for the inline and crossline samples size, and the second number defining the vertical number of samples. In Figures 9 and 10, we show the displays on using the parameters as 1×5 (Figure 9a), 2×9 (Figure 9b), 3×10 (Figure 10a), and 5×10 (Figure 10b). The use of higher values of the parameters tends to smooth out the detail on the curvature displays.

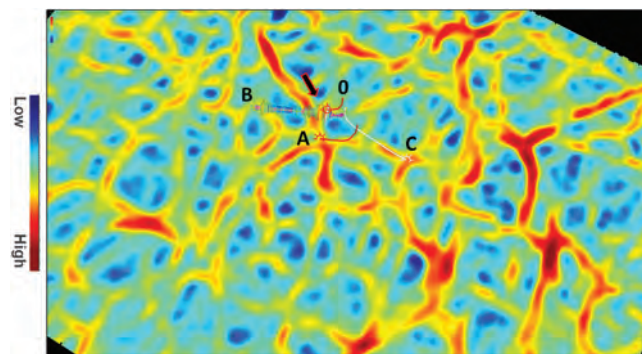


Figure 13. Horizon map display for most-positive curvature attribute generated using the Gaussian-weighted method using 2×9 as the parameters, shown correlated with the fracture density log at the location of the black arrow. Notice that the correlation of the bigger fracture density disc with the curvature lineament at that location is not as good. The curvature data in Figures 13–15 use a different color bar than the previous figures. The high-resolution image log fracture density log continues to be illustrated with the old color bar of Figure 1 (data courtesy of SEI, Canada).

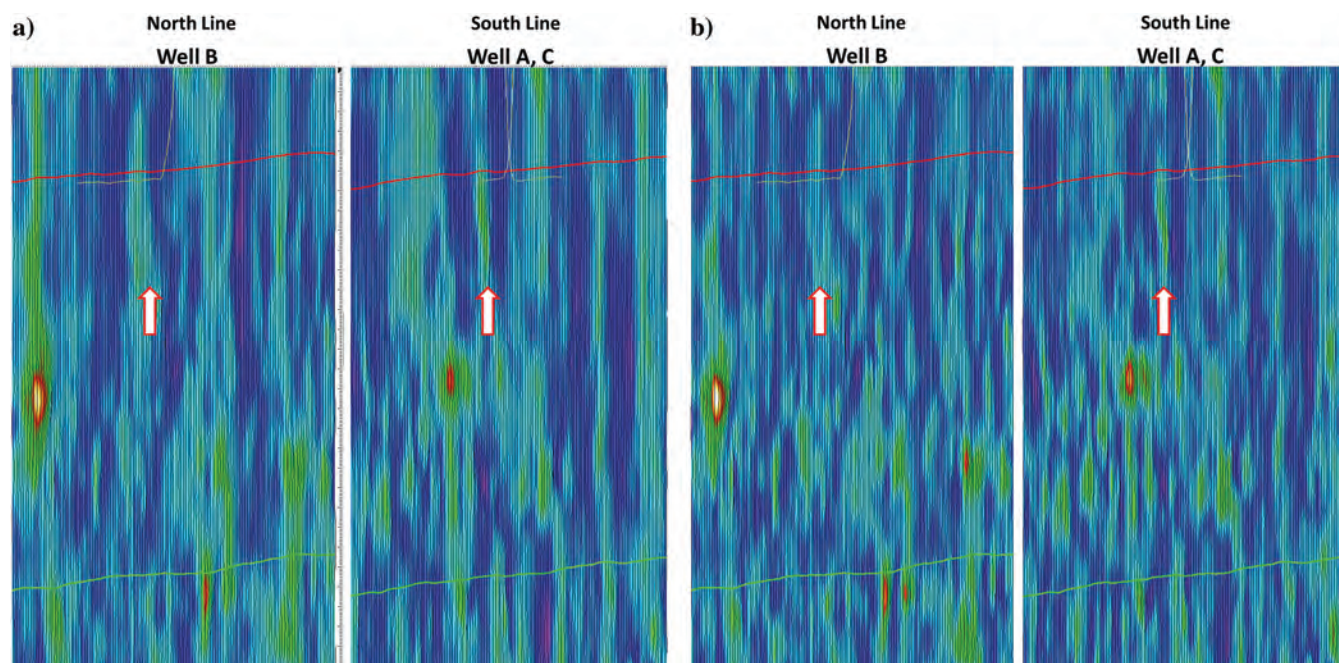


Figure 12. Segments of the north and south lines shown in Figure 1b from the most-positive curvature volume generated using a Fourier filtering algorithm using an alpha value of (a) 0.65 and (b) 0.8. Using higher values of the alpha parameter increases the detail, and perhaps the noise, on the curvature displays (data courtesy of SEI, Canada).

Finally, we use the Fourier-filtering algorithm as described above using an optimized choice of five samples in the inline and crossline directions and using 22 ms in the vertical directions. In Figures 11 and 12, we show the line displays with values of the fractional index as 0.2 (Figure 11a), 0.4 (Figure 11b), 0.65 (Figure 12a), and 0.8 (Figure 12b). As expected as we go from lower to higher values of the fractional index, we see more and more resolution of the curvature detail. In contrast to the unfiltered results, the Fourier filtered results are stable for very small ($5 \times 5 \times 22$ ms) cuboids, which is critical if time localization is important.

In Figure 13, we show the equivalent horizon slice displays from the most-positive curvature attributes generated using the Gaussian-filtering algorithm, and

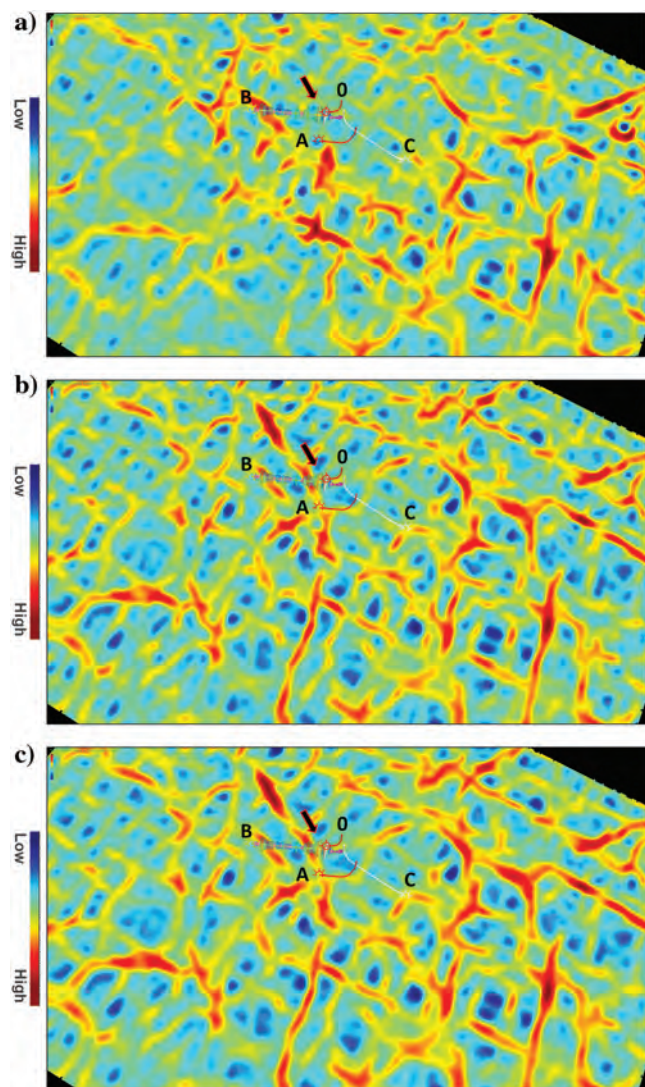


Figure 14. Horizon map display for most-positive curvature attribute generated using the linear-weighted method with (a) $9 \times 9 \times 22$ ms, (b) $9 \times 9 \times 98$ ms, and (c) $11 \times 11 \times 98$ ms, shown correlated with the fracture density log at the location of the black arrow. Notice that the correlation of the fracture density discs with the red curvature lineament is not that good (data courtesy of SEI, Canada).

use of 2×9 as the parameter choice. We notice that the correlation of the bigger fracture density disc with the curvature lineament at that location is not as good, but the arcuate feature we expected from the diffraction imaging interpretation is present.

Similarly, in Figure 14, we show the equivalent horizon slice from the most-positive curvature attributes generated using the linear-weighted algorithm, with $9 \times 9 \times 22$ ms (Figure 14a), $9 \times 9 \times 98$ ms (Figure 14b), and $11 \times 11 \times 98$ ms (Figure 14c) as the parameters. Again, we notice that the correlation of the fracture density discs with the different curvature lineaments is not as good. The arcuate feature we expected from the diffraction imaging is not apparent in Figure 14a, in which

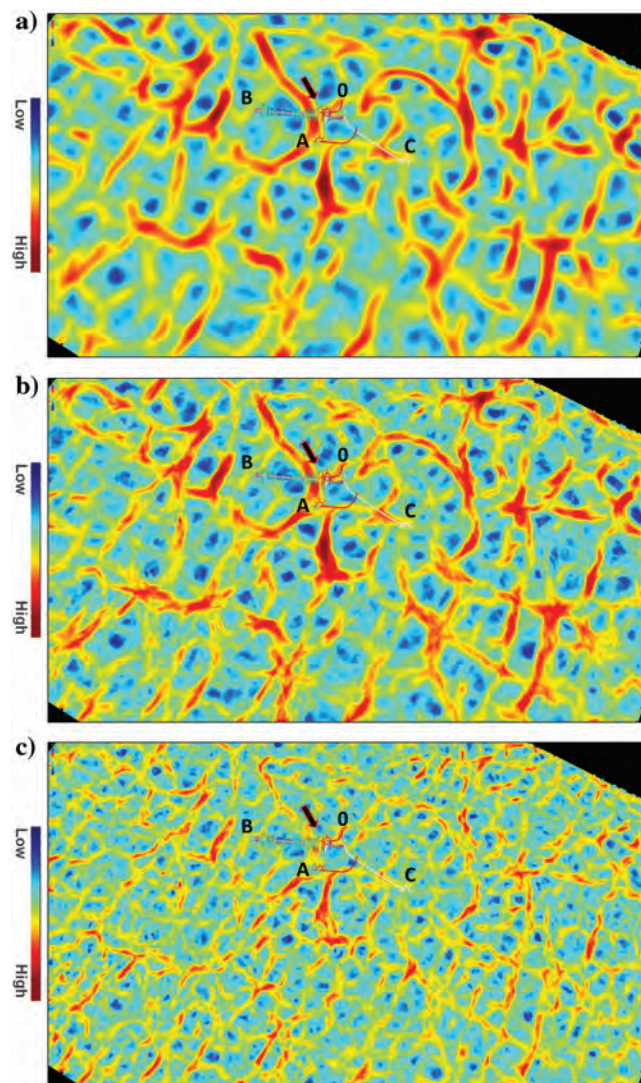
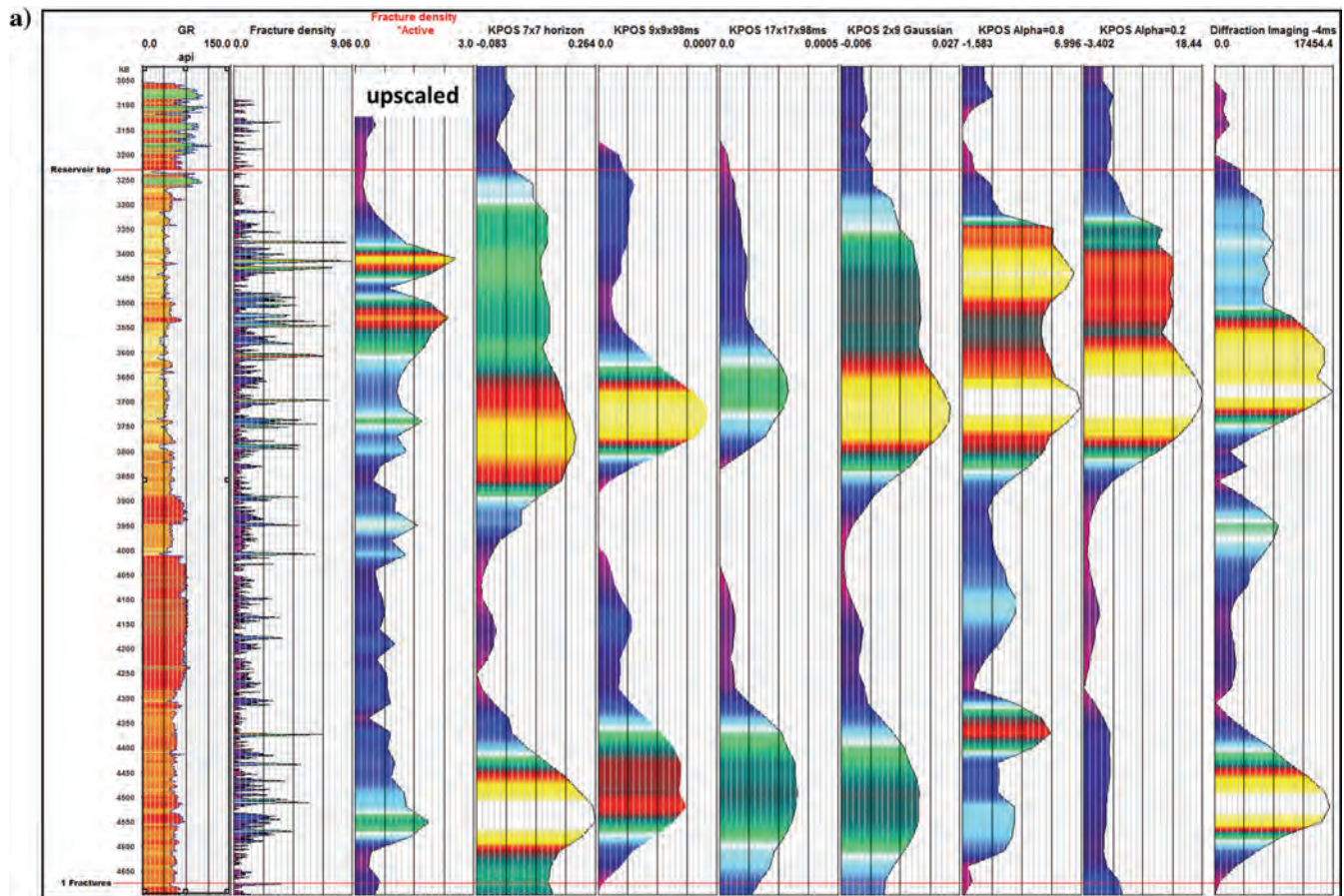


Figure 15. Horizon map display for most-positive curvature attribute generated using the Fourier-filtering method with a fractional index value of (a) 0.2, (b) 0.65, and (c) 0.8, shown correlated with the fracture density log at the location of the black arrow. Notice the good correlation of the fracture density discs with the red curvature lineament at that location, although we also notice that with the decreasing value of alpha, the lineament detail gets smoothed out (data courtesy of SEI, Canada).



b)

Description of curvature algorithm and parameters		Correlation coefficients	Qualitative evaluation	
Type of algorithm	Parameters - all KPOS	With fracture density, 55 samples	Map response	Line response
Linear weighted cuboid (Unfiltered)	3x3x98	-.104	unuseable	unuseable
	5x5x98	-.045	poor	poor
	7x7x98	.168	good-noisy	good-noisy
	9x9x22	.100	poor	poor
	9x9x46	.185	poor	poor
	9x9x98	.263	good	good
	11x11x98	.295	good	good
Gaussian weighted cuboid	17x17x98	.308	degrading	degrading
	1x5	.516	poor	poor
	2x9	.527	good	good
	3x10	.515	good	good
	5x10	.483	degrading	degrading
Fourier filtered 5x5x22ms cuboid	Alpha 0.8	.597	degraded?	degraded?
	Alpha 0.65	.565	good	good
	Alpha 0.5	.375	good	good
	Alpha 0.4	.375	good	good
	Alpha 0.2	.509	good	good
	Alpha 0.2 50ms window	.439	degraded	degraded
	Alpha 0.4 50ms window	.415	degraded	degraded
	Alpha 0.8 50ms window	.390	degraded	degraded

Figure 16. Quantitative comparison of results. (a) Gamma ray log, original and upscaled fracture density from image log data, and most-positive curvature with different methods for the horizontal length of well B. (b) A results summary with a roll-up of the correlations to fracture density as well as the qualitative line and map-based evaluations. Correlation coefficients passing the 1% *p*-test for significance are colored dark yellow.

a short time window is used. This 22 ms short time window result is qualitatively similar to the horizon-based results of Figure 3.

In Figure 15, we show the horizon slice comparison from the most-positive curvature attributes generated using the Fourier-filtering algorithm, with values of fractional index as 0.2 (Figure 15a), 0.65 (Figure 15b), and 0.8 (Figure 15c). Each of these displays is shown correlated with the fracture density log at the location of the black arrow. As the values of the fractional index increase, we see an increasing level of lineament detail on the curvature displays. The image log fracture density as shown along the lateral of well B along with the position of the toes of well 0 and well A are important considerations in this figure because interpretability was based on the expected arcuate or linear curvature feature connecting the toes of well 0, well A and the high fracture densities from well B.

All of the results, except for the horizon-based one, show the expected high most-positive curvature trend, although some details change in the complexity of the trend. The horizon-based map of Figure 3a was considered poor because it was dominated by pick-based artifacts. The unfiltered $9 \times 9 \times 98$ ms volumetric result of Figure 14b appears quite interpretable on map view, although smaller time windows gave poor results. The Gaussian-filtered volumetric result is shown in Figure 13, and it is not materially dissimilar to the unfiltered result. The Fourier-filtered result ($5 \times 5 \times 22$ ms) with a fractional index parameter of 0.2 is shown in Figure 15a, and it is considered excellent, especially in its preservation of curved features.

Quantitative comparisons

Linear regression was performed between the most-positive curvature maps and the fracture densities from the image log along the lateral of well B. Figure 16 shows the log comparison and the correlation coefficients, and it rolls up the overall evaluation of the parameter test. Figure 16a shows the values of curva-

ture, diffraction imaging, and fracture density in a log format. There are 55 seismic-sized samples along the lateral, so once the fracture density data are upsampled, it can be correlated with all of the seismic attributes. The entire set of correlation results is summarized in Figure 16b. The Fourier-filtered results were the most robust to parameterization and were stable at small cuboid sizes. The Gaussian-filtered results seemed decent for all but the smallest and largest parameters tested. The unfiltered volumetric approach required very large time windows, which was related to the localization of the interpretation for fractures. The horizon-based method suffered from pick-based artifacts in most comparisons. We tabulate all these results in Table 1.

Conclusion

We revisited the question of curvature window size and filtering method for the estimation of fractures, and we found that these parameters can be of material operational importance. Our work suggests that the best parameters should not be assumed. We used a variety of methods to evaluate which parameterizations were best, which included quantitative and qualitative techniques. Among the qualitative techniques was an appeal to the independent edge-detecting method of diffraction imaging. The volume-based curvature approaches seemed better in map evaluation than the horizon-based estimates, although the smallest xyz cuboid size of the volumetric estimates tended to bear greater similarity to the horizon solutions. Filtering of the curvature results was also material to the evaluation of the risk from natural fractures, with the Fourier-based filtering showing the most robustness to different parameterization. Of the volume-based methods, the unfiltered approach was most problematic to effective interpretation, requiring bigger time windows for stability. Evaluation of the best parameterization of curvature required the use of objective correlations to the interpretive target as well as more subjective map and line comparisons. Based on the interpretation of fractures, there appeared

Table 1. Results summary.

Type of algorithm	Parameter	Map response	Line response	Correlations
Horizon based	Small (9×9)	Artifacts	N.A.	Significant
	Big (17×17)	Less artifacts	N.A.	Significant
Linear-weighted cuboid	Very small xy , long time	Poor	Poor	Insignificant
	Small xy , long time	Good	Good	Insignificant
	Large xy , long time	Good washed?	Washed out	Significant
	Shorter time windows	Degrades	Degrades	Insignificant
Gaussian-weighted cuboid	Small	Poor	Poor	Significant
	Medium	Good	Good	Significant
Fourier filtered, small xyz cuboid	High spatial frequency (small)	Good	Good	Significant
	Low spatial frequency (big)	Good	Good	Significant
	Bigger time windows	Relatively poor	Degrades	Significant

to be a sweet spot size for the cuboid or filtering for each of the volumetric approaches. A rational approach to choosing the parameters for curvature requires the consideration of the interpretive objective or target, as “best” is inextricably bound by purpose.

Acknowledgments

Seismic data are owned or controlled by Seismic Exchange Inc.; the interpretation is that of Jupiter Resources Inc. We thank SEI Canada for permission to show certain images of data licensed from them.

References

- Al-Dossary, S., and K. J. Marfurt, 2006, 3D volumetric multi-spectral estimates of reflector curvature and rotation: *Geophysics*, **71**, no. 5, P41–P51, doi: [10.1190/1.2242449](https://doi.org/10.1190/1.2242449).
- Chopra, S., and K. J. Marfurt, 2007, Volumetric curvature attributes adding value to 3D seismic data calibration: *The Leading Edge*, **26**, 856–867, doi: [10.1190/1.2756864](https://doi.org/10.1190/1.2756864).
- Fomel, S., E. Landa, and T. Taner, 2007, Poststack velocity analysis by separation and imaging of seismic diffractions: *Geophysics*, **72**, no. 6, U89–U94, doi: [10.1190/1.2781533](https://doi.org/10.1190/1.2781533).
- Hennings, P. H., J. E. Olson, and L. B. Thompson, 2000, Combining outcrop data and three dimensional structural models to characterize fractured reservoirs: An example from Wyoming: *AAPG Bulletin*, **84**, 830–849.
- Hunt, L., 2013, The importance of making conclusions and frameworks in reasoning: *CSEG Recorder*, **38**, 56–60.
- Hunt, L., R. Reynolds, T. Brown, S. Hadley, J. Downton, and S. Chopra, 2010, Quantitative estimate of fracture density variations in the Nordegg with azimuthal AVO and curvature: A case study: *The Leading Edge*, **29**, 1122–1137, doi: [10.1190/1.3485773](https://doi.org/10.1190/1.3485773).
- Hunt, L., R. Reynolds, S. Hadley, J. Downton, and S. Chopra, 2011, Causal fracture prediction: Curvature, stress, and geomechanics: *The Leading Edge*, **30**, 936–948.
- Keating, D. P., and M. P. Fischer, 2008, An experimental evaluation of the curvature-strain relation in fault related folds: *AAPG Bulletin*, **92**, 869–884, doi: [10.1306/03060807111](https://doi.org/10.1306/03060807111).
- Klokov, A., and S. Fomel, 2012, Separation and imaging of diffractions using migrated dip-angle gathers: *Geophysics*, **77**, no. 6, S131–S143, doi: [10.1190/geo2012-0017.1](https://doi.org/10.1190/geo2012-0017.1).
- Koren, Z., and I. Ravve, 2011, Full-azimuth subsurface angle domain wavefield decomposition and imaging. Part 1: Directional and reflection image gathers: *Geophysics*, **76**, no. 1, S1–S13, doi: [10.1190/1.3511352](https://doi.org/10.1190/1.3511352).
- Landa, E., 2012, Seismic diffraction: What's the value?: 82nd Annual International Meeting, SEG, Expanded Abstracts, doi: [10.1190/segam2012-1602.1](https://doi.org/10.1190/segam2012-1602.1).
- Murray, G. H., 1968, Quantitative fracture study — Sanish Pool, McKenzie County, North Dakota: *AAPG Bulletin*, **52**, 57–65.
- Nelson, R., 2001, *Geologic analysis of naturally fractured reservoirs*: Elsevier.

- Roberts, A., 2001, Curvature attributes and their application to 3D interpreted horizons: *First Break*, **19**, 85–100, doi: [10.1046/j.0263-5046.2001.00142.x](https://doi.org/10.1046/j.0263-5046.2001.00142.x).



Lee Hunt received a B.S. (1990) in geophysics from the University of Alberta, after which he started his career working for PanCanadian Petroleum Ltd. He was the 2011/2012 CSEG distinguished lecturer, and he is one of the founding members of the value of integrated geophysics steering committee. His experience ranges

from interpretation to managing a business unit, and he has conducted numerous winter-access-only drilling campaigns in the northeast part of British Columbia (NEBC) and Northern Alberta. He has drilled more than 350 wells in most of the play types within the Western Canadian Sedimentary Basin. These drilling experiences include heavy oil, shallow gas, deep carbonate exploration, deep basin, Peace River Arch, Saskatchewan and Manitoba oil, and they include vertical as well as horizontal drilling. His work has focused on performing quantitative analysis of multiple attenuation, resolution enhancement, depth and geohazard predictions, AVO, AVAz, VVAz, curvature, and the prediction of fluid, lithology, porosity, fracture treatment characteristics, and production. He and his coauthors won the Excellence of Oral Presentation for the 1997 SEPM Convention award, the 2000 CSEG Convention Best Paper Award, the 2008 CSEG Convention Best Geophysical Abstract, the 2008 CSEG Best Technical Luncheon Talk, the 2010 CSEG Convention Best Geophysical Oral Presentation, the Best Exploration Paper at VII INGPET in 2011, Honorable Mention for Best Paper in *The Leading Edge* in 2011, and Best Paper in the *CSEG Recorder* in 2011. He was a participant in the creation of the CSEG MLA, APEGGA's Q.I. Practise Standard, as well as APEGGA's Guideline for the Ethical Use of Geophysical Data. He is one of the principal designers of the CSEG Value of Geophysics with Case Histories course.



Bahaa Beshry received a B.S. (2007) in geophysics from the University of Calgary. Upon graduation, he began a full time career with Encana Corporation, where he worked several different assets, including the Deep Basin Alberta and NEBC. Recently, he spent two years at Jupiter Resources, where he has continued working in the deep basin of Alberta — some of his work includes drilling and geosteering of 25 horizontal wells. He was also involved in managing the reprocessing and merging of 16 separate 3D seismic surveys to increase the consistency of amplitude, phase, and structure across several volume boundaries, improve the imaging of deep and shallow formations, as well as increasing the confidence of our well inventory. His work at Jupiter has also continued through focusing on depth and geohazard predictions, AVO analysis, 3D curvature, VVAz,

and the prediction of lithology and porosity using geologic parameters.



Satinder Chopra has 34 years of experience as a geophysicist specializing in processing, reprocessing, special processing, and interactive interpretation of seismic data. He has rich experience in processing various types of data such as vertical seismic profiling, well-log data, seismic data, etc., as well as excellent communication skills, as evidenced by the many presentations and talks delivered and books, reports, and papers he has written. He has been the 2010–2011 CSEG Distinguished Lecturer, the 2011–2012 AAPG/SEG Distinguished Lecturer, and the 2014–2015 EAGE e-Distinguished Lecturer. He has published eight books and more than 400 papers and abstracts and likes to make presentations at any beckoning opportunity. His work and presentations have won several awards, the most notable ones

being the EAGE Honorary Membership (2017), CSEG Honorary Membership (2014) and Meritorious Service (2005) Awards, 2014 Association of Professional Engineers and Geoscientists of Alberta (APEGA) Frank Spragins Award, the 2010 AAPG George Matson Award, and the 2013 AAPG Jules Braunstein Award, SEG Best Poster Awards (2007, 2014), CSEG Best Luncheon Talk Award (2007), and several others. His research interests focus on techniques that are aimed at the characterization of reservoirs. He is a member of SEG, CSEG, CSPG, EAGE, AAPG, and APEGA.



Cole Webster received a B.S. honours (2005) in geologic science from the University of Saskatchewan. He began his career at Encana and spent nine years there before moving to Jupiter Resources, where he has spent the last three years. He is currently a senior geologist at Jupiter with a focus on development in the Resthaven area.